Trigger and Calorimeter Data Acquisition of the High-Energy Particle Detector Onboard the CSES-02 Satellite

Antonio Anastasio, Simona Bartocci, Roberto Battiston, Stefania Beolè, Franco Benotto, Alfonso Boiano, Piero Cipollone, Silvia Coli, Andrea Contin, Marco Cristoforetti, Cinzia De Donato, Cristian De Santis, Andrea Di Luca, Flori Dumitrache, Francesco Maria Follega, Simone Garrafa Botta, Giuseppe Gebbia, Roberto Iuppa, Alessandro Lega, Mauro Lolli, Giuseppe Masciantonio, Vincenzo Masone, Matteo Mergè, Marco Mese, Riccardo Nicolaidis, Francesco Nozzoli, Alberto Oliva, Giuseppe Osteria, Francesco Palma, Federico Palmonari, Beatrice Panico, Stefania Perciballi, Francesco Perfetto, Piergiorgio Picozza, Michele Pozzato, Ester Ricci, Marco Ricci, Sergio Bruno Ricciarini, Zouleikha Sahnoun, Umberto Savino, Valentina Scotti, *Senior Member, IEEE*, Enrico Serra, Alessandro Sotgiu, Roberta Sparvoli, Pietro Ubertini, Antonio Vanzanella, Veronica Vilona, Simona Zoffoli, and Paolo Zuccon

***Abstract*— This article describes the innovative system performing the trigger and the readout of the photomultiplier tubes (PMTs) for the high-energy particle detector (HEPD) onboard the second satellite of the China Seismo Electromagnetic Satellite (CSES) mission. The second HEPD is designed to measure cosmic rays covering an energy spectrum ranging from a few megaelectronvolts to several hundreds of megaelectronvolts. This high-precision detector consists of different subsystems: a solid-state tracker, a segmented trigger, a calorimeter composed of a tower of plastic scintillators, and two layers of lutetium-yttrium oxyorthosilicate (LYSO) crystals, along with a containment detector. The data acquisition (DAQ) process for the trigger, calorimeter, and containment detector is carried out by a single electronic board, relying on two Weeroc CITIROC application-specific integrated circuits (ASICs), which are being utilized in space for the first time. This board also generates and manages trigger signals for the entire detector. It effectively captures signals with distinct timing characteristics from plastic scintillators and inorganic crystals. Given the wide range of particle fluxes encountered during CSES's orbit, adaptability of the trigger generation system becomes crucial, and DAQ is optimized to ensure consistent energy spectra measurement with a substantial duty cycle. The trigger system of the second HEPD implements concurrent trigger patterns and the ability to select DAQ strategies based on orbital zones and the presence of impulsive events. Each trigger configuration is designed to meet scientific demands concerning the field of view and the characteristics of the particles reaching the detector, with prescaling settings fine-tuned accordingly. In addition to monitoring particle bursts, trigger configurations specific to gamma rays will be tracked in 5-ms intervals to measure photon fluxes in the energy range from 2 to 20 MeV and provide sensitivity for impulsive events, such as gamma-ray bursts (GRBs). This article provides a comprehensive account of the design criteria, the architectural choices specifically adapted for space applications, and the original trigger management strategy. Additionally, this article presents an in-depth analysis of the performance of the trigger system and comprehensive results from laboratory and beam tests conducted on the qualification and flight models of second HEPD.**

***Index Terms*— Astroparticle physics, data acquisition (DAQ), detectors, front-end electronics, space instrumentation.**

Received 8 November 2024; revised 7 March 2025; accepted 9 March 2025. Date of publication 28 March 2025; date of current version 24 April 2025. This work was supported in part by Italian Space Agency in the framework of the "Accordo Attuativo 2020-32.HH.0 Limadou Scienza+" under Grant CUP F19C20000110005; and in part by the Italian Space Agency (ASI)-Italian National Institute for Nuclear Science (INFN) under Agreement 2014-037-R.0, addendum 2014-037-R-1-2017. The Associate Editor coordinating the review process was Dr. George Dan Mois. *(Corresponding author: Valentina Scotti.)*

Antonio Anastasio, Alfonso Boiano, Vincenzo Masone, Giuseppe Osteria, Francesco Perfetto, and Antonio Vanzanella are with INFN-Sezione di Napoli, 80126 Naples, Italy.

Simona Bartocci is with INFN-AC, 00044 Frascati, Italy.

Roberto Battiston, Francesco Maria Follega, Giuseppe Gebbia, Roberto Iuppa, Alessandro Lega, Riccardo Nicolaidis, Ester Ricci, and Paolo Zuccon are with the Università di Trento, 38122 Trento, Italy, and also with INFN-TIFPA, 38123 Trento, Italy.

Stefania Beolè, Stefania Perciballi, and Umberto Savino are with the Università di Torino, 10125 Turin, Italy, and also with INFN-Sezione di Torino, 10125 Turin, Italy.

Franco Benotto, Silvia Coli, Flori Dumitrache, and Simone Garrafa Botta are with INFN-Sezione di Torino, 10125 Turin, Italy.

Piero Cipollone, Cinzia De Donato, Cristian De Santis, Giuseppe Masciantonio, Francesco Palma, and Alessandro Sotgiu are with INFN-Sezione di Roma Tor Vergata, 00133 Rome, Italy.

Andrea Contin, Federico Palmonari, and Zouleikha Sahnoun are with the Università di Bologna, 40126 Bologna, Italy, and also with INFN-Sezione di Bologna, 40127 Bologna, Italy.

Marco Cristoforetti and Andrea Di Luca are with the Fondazione Bruno Kessler, 38122 Trento, Italy, and also with INFN-TIFPA, 38123 Trento, Italy.

Mauro Lolli, Alberto Oliva, and Michele Pozzato are with INFN-Sezione di Bologna, 40127 Bologna, Italy.

Matteo Mergè and Simona Zoffoli are with Italian Space Agency, 00133 Rome, Italy.

Marco Mese, Beatrice Panico, and Valentina Scotti are with the Department of Physics (E. Pancini), Università degli Studi di Napoli, 80126 Naples, Italy, and also with INFN-Sezione di Napoli, 80126 Naples, Italy (e-mail: scottiv@na.infn.it).

Francesco Nozzoli, Enrico Serra, and Veronica Vilona are with INFN-TIFPA, 38123 Trento, Italy.

Piergiorgio Picozza and Roberta Sparvoli are with the Universita di Roma Tor Vergata, 00133 Rome, Italy, and also with INFN-Sezione di Roma Tor Vergata, 00133 Rome, Italy.

Marco Ricci is with INFN-LNF, 00044 Frascati, Italy.

Sergio Bruno Ricciarini is with IFAC-CNR, 50019 Sesto Fiorentino, Italy.

Pietro Ubertini is with INAF-IAPS, 00133 Rome, Italy.

Digital Object Identifier 10.1109/TIM.2025.3555671

I. Introduction

THE China Seismo Electromagnetic Satellite (CSES) space program is designed to study ionospheric

© 2025 The Authors. This work is licensed under a Creative Commons Attribution 4.0 License.
For more information, see https://creativecommons.org/licenses/by/4.0/

perturbations of electromagnetic field, plasma, particles, and their correlation with seismic phenomena and consists of several multipayload satellites. It aims to investigate particle or electromagnetic disturbances in the ionosphere and their possible correlation with seismic activity [1]. The CSES-01 satellite, the first of the constellation, has been working since February 2018 [2]. The payloads onboard this satellite are not designed to acquire data on the whole orbit: in the payload operating zone (latitude range of +/−65°), the detectors acquire data, while in the platform adjustment zone, all instruments are turned out to execute the activities of the satellite attitude and orbit control system.

Some of the first results from CSES-01 include the detection of the G3 geomagnetic storm of August 26, 2018 [3] and the observations of the Bayan earthquake on August 5, 2018 [4]. Data collected also have been used for the retrospective analysis of high-magnitude seismic events, such as the Palu earthquake on September 28, 2018 ($M_W = 7.5$) and the Papua New Guinea earthquake on May 14, 2019 ($M_W = 7.6$). These analyses found several ionospheric anomalies that could be related to the preparation phase of these seisms [5]. Additionally, the first high-energy particle detector (HEPD)-01 has proven the effectiveness of these detectors in describing the radiation environment surrounding Earth [6], [7], [8]. This includes identifying the trapped radiation in the South Atlantic Anomaly (SAA), monitoring solar activity by detecting solar energetic particles (SEPs) [9], and detecting gamma-ray bursts (GRBs) [10], [11], [12].

The CSES-02 satellite will be launched at the end of 2024 on a sun-synchronous polar orbit at a 507-km altitude, with a 97° inclination; all the payloads on the satellite will operate continuously. The CSES-02 orbit will be shifted 180° compared to the one of CSES-01, to reduce the time gap between two passages over the same location.

This article describes the main characteristics of the trigger and calorimeter acquisition board of the HEPD-02, focusing on the improvements and upgrades to the HEPD-01 [13]. A preliminary description of the trigger and DAQ system of HEPD-02 has been presented in [14]; here, we will provide a thorough characterization of the board and its functionalities.

The HEPD-02 is designed to detect particles in the 3–200-MeV energy range [15]. It measures the type, energy, and pitch angle of individual particles. It aims to investigate seismo-induced disturbances within the inner Van Allen belt, along with the study of the Sun activity and cosmic ray solar modulation [16]. The detector presents an improved structure to lower the energy threshold of particle detection and a new tracking system, within the usual space limitation in weight and power consumption.

The HEPD-02 is composed of several subsystems (Fig. 1) as follows.

1) *Trigger:* Two segmented layers of plastic scintillator (EJ-200), which contains the direction detector. The segments of the first layer (TR1 in Fig. 1) are arranged perpendicularly to the segments of the second layer (TR2).
2) *Direction Detector:* Three planes of complementary metal–oxide–semiconductor (CMOS) and monolithic active pixel sensor. By using the (x, y) hit coordinates measured by the three planes, the particle track can be reconstructed in 3-D space. The direction detector is segmented into five turrets, and each turret is aligned with one of the segments of TR1.
3) *Energy Detector:* A range calorimeter composed of 12 planes of plastic scintillators (10 mm), followed by two crossed planes of lutetium-yttrium oxyorthosilicate (LYSO) crystals (EN1-2), each segmented into three bars. The LYSO has been chosen for its higher light yield, which enhances the energy range of the detector.
4) *Containment Detector:* Composed of four lateral (LAT_01, LAT_02, LAT_03, and LAT_04) and one bottom (BOT) panels of plastic scintillators (8 mm). This detector allows to reject particles not fully contained in the calorimeter.

All scintillators are coated with a reflective layer, and each counter is connected with two Hamamatsu R9880-210 photomultiplier tubes (PMTs) for a total of 64 channels. The PMTs are positioned on opposite sides or corners of the counters to obtain a uniform light collection.

Significant enhancements were implemented in both the tracker and the trigger detectors, compared to those installed in the HEPD-01. The trigger subdetector has been redesigned to handle the higher particle fluxes that will be experienced at high latitudes. For a better alignment with the tracker, the first layer of the trigger (TR1 in Fig. 1) is divided into five bars, each of which is read through light guides connected to PMTs. The light guides are crafted to align with the shape of the scintillator bar and the phototube's aperture, maximizing light collection efficiency. The first plane's thickness has been set at 2 mm to reduce multiple scattering and to allow a low detection threshold.

The second trigger layer (TR2 in Fig. 1) is divided into four thicker segments (8 mm) to estimate the energy loss of charged particles accurately.

In addition to the improvements made to the detector, the trigger system logic has been completely redesigned to offer greater versatility [17]. Various trigger configurations, created by combining signals from the two trigger layers and multiple calorimeter planes, can be chosen during the flight. Additionally, the logic implements adjustable prescaling factors to enable a stringent selection of incoming particles to handle the high fluxes encountered in polar orbits, as will be discussed in Section IV.

II. Electronics of the HEPD-02

The HEPD-02 electronics consists of five primary boards, and the connections among them are schematically depicted in Fig. 2 as follows.

1) *Tracker DAQ (T-DAQ):* It acquires and processes data from the tracker [18].
2) *Trigger Board:* It reads out all the scintillator detectors (trigger, energy detector, and containment detector),

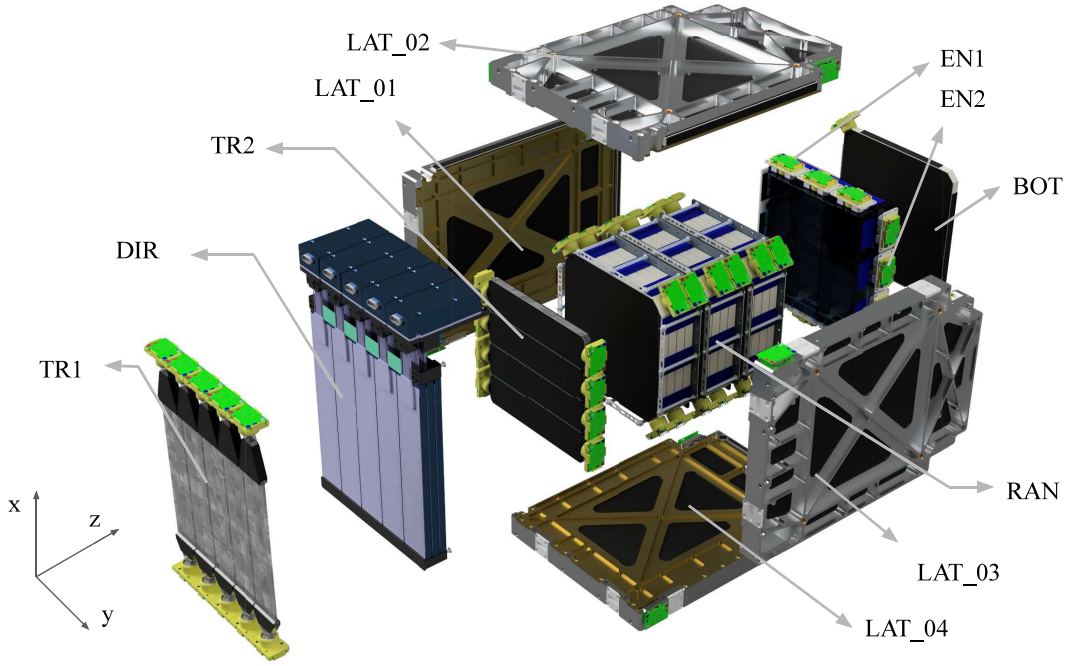

Fig. 1. Exploded view of the HEPD-02 subdetectors: trigger planes (TR1 and TR2), CMOS tracker (direction detector), energy detector, composed of a plastic scintillator tower (RAN), a LYSO calorimeter (EN), and containment detector (LAT and BOT).

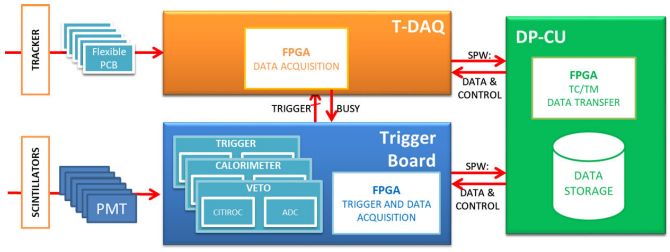

Fig. 2. Diagrammatic representation of the HEPD-02 electronics.

manages signals coming from the PMTs, and generates the trigger necessary to begin and control the whole DAQ [19].

3) *Data Processing and Control Unit (DPCU):* It collects data from the T-DAQ and the Trigger Board and controls the instrument and the communication with the satellite platform.
4) *High-Voltage Control Board (HV-CTRL):* It controls the power supply of the PMTs.
5) *Low-Voltage Control Board (LV-CTRL):* It controls the power supply of the rest of the detector.

A dedicated mechanics box houses the electronic components and allows anchoring to the HEPD-02 base plate and heat dissipation. All boards meet design requirements for low power consumption, passive heat dissipation, radiation tolerance, and a redundant design. The redundancy is achieved by creating two duplicates and autonomous sections for each board. If a significant malfunction arises in the primary section (HOT), it can be deactivated and the secondary (COLD) can be employed. Additionally, all components have been selected to operate effectively over an extended temperature range (−40 °C to 85 °C).

The boards communicate with the DPCU via SpaceWire protocol, while the communication with the satellite is established via CANBUS and RS-422 protocols. The maximum data transfer rate available from the satellite, 100 Gbit/day, limits the amount of storable data and the maximum acceptable trigger rate.

III. Trigger Board

The key features of the Trigger Board are as follows.

1) Readout and digitization of 64 PMTs' signals using two 32-channel application-specific integrated circuits (ASICs) CITIROC (Weeroc).
2) Adjustable gain and trigger threshold for optimization of the acceptance.
3) Two different configurable gain chains.
4) Provide prescalable and concurrent trigger configurations to optimize sensitivity across various orbital zones and energy ranges.
5) Implement rate meters for each PMT and trigger configuration.

Fig. 3 shows a schematic description of the Trigger Board. Due to the high particle fluxes expected in the polar regions and the SAA, the Trigger Board design for the HEPD-02 required enhanced trigger logic and the implementation of prescaling factors. Additionally, with longer orbit sessions dedicated to science operations, a greater volume of data will be collected, necessitating onboard mass memory for buffering and an increased data budget. To improve signal measurement from the LYSO, which has slower response times compared to

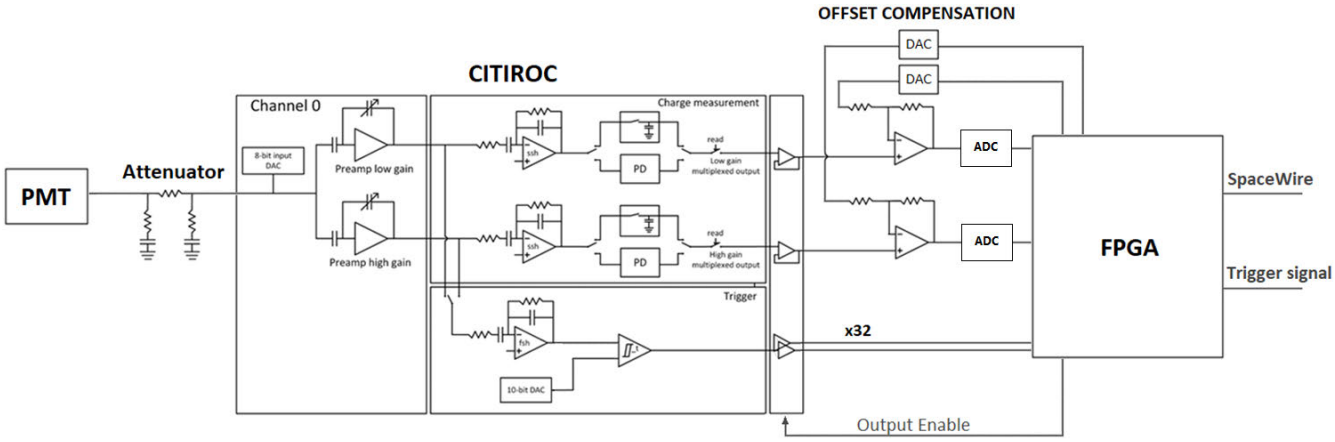

Fig. 3. Schematic block diagram of the Trigger Board.

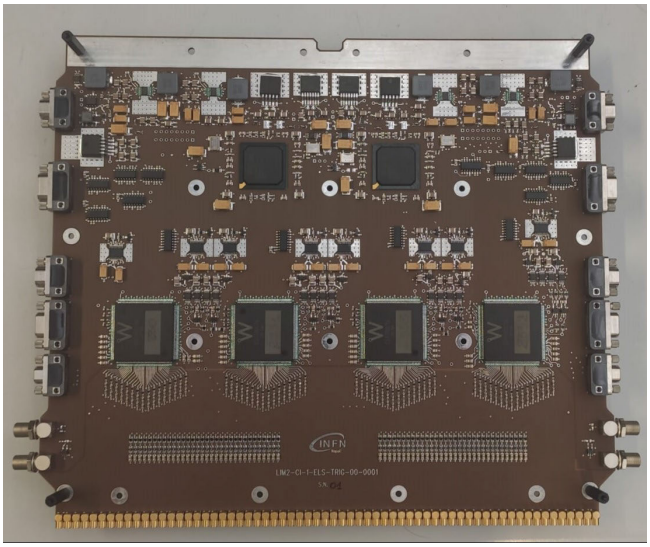

Fig. 4. Qualification model of the Trigger Board of the HEPD-02. The 64 input channels on the bottom of the board are shared by the HOT and COLD sections. Each section is equipped with one FPGA and two CITIROC chips by Weeroc.

the plastic scintillators, the read-out ASICs have been updated relative to those used in the HEPD-01, allowing for the use of peak detector, as described in the following paragraphs.

The Trigger Board has been specifically designed by the INFN Naples Division. The board is divided into two identical sections, called HOT and COLD (see Fig. 4). Only the HOT side is normally powered while the other is used only in the case of failures. Each section features a Microsemi A3PE3000L field-programmable gate array (FPGA) that implements the logic and two CITIROC ASICs [20] by Weeroc to collect the signals coming from the PMTs and four ADCs (AD7274, 12 bits, 24 MHz). All the 64 channels are in common for HOT and COLD sections using two identical conditioning circuits carefully designed to split the signal from PMTs to the two sections.

A. FPGA Firmware

Most of the functionalities of the Trigger Board are implemented through the FPGA, and the general architecture of the firmware can be divided into the following functional modules.

1) *Clock Management:* It provides a series of clock dividers that allow the generation of the several internal clocks. Since the board had to meet the requirements for operation in space, it was not possible to use a phase-locked loop (PLL) to produce all the clocks due to its radiation sensitivity, the use of dividers, and two different oscillators.
2) *Power and Watchdog Control:* It enables the regulators connected to the analog and digital power sections of CITIROCs. When the Trigger Board turns on, the CITIROCs are not powered to avoid excessive absorption peaks during the start-up.
3) *Signal Synchronizers and Extenders:* External signals (such as triggers from CITIROCs or the BUSY from DPCU and TDAQ) are synchronized with the internal clock using a series of dual flip-flop synchronizers. To ensure a correct sampling, these signals are also extended to 100 ns.
4) *SpaceWire Controller:* The communication with the other boards is based on the SpaceWire protocol. This module decodes the serial signals into a sequence of addresses and data. A finite-state machine (FSM) stores data in a series of 32-bit internal registers (see Section III-C).
5) *CITIROC Offset Compensation Controller:* It removes the offset of the analog output of the CITIROCs and amplifies the voltage to adapt it to the input dynamic range of the ADCs.
6) *FCounters:* To measure trigger rates and the alive and dead time of the detector, in addition, a pulse per second counter is used to synchronize data between the subsystems of HEPD-02.
7) *Temperature Sensor Controller:* It manages two AD7814 temperature sensors, placed in regions of the board that are supposed to be the hottest during the operation.
8) CITIROC configuration FSM.
9) Trigger logic and ADC readers.

The last two items will be discussed in detail in Sections III-B and III-C.

TABLE I
ATTENUATION FACTORS FOR THE INPUT CHANNELS OF THE TRIGGER BOARD

Board channels	Scintillators	Attenuation
0 - 4, 32 - 36	TR1	6
5 - 31, 37 - 63	TR2, RAN, EN, BOT, LAT	12

B. PMT Data Collection and Trigger

Signals from PMTs are collected from the last dynode, to have positive signals to match the input polarity of CITIROCs. This also allows reducing the power consumption and simplifies the design since it avoids the usage of inverters. The signals from the PMTs are transmitted through RG178 coaxial cables to enhance noise immunity. A conditioning stage has been implemented to scale the PMTs' signals and make them compatible with the CITIROC input dynamic range. This has been implemented using resistive voltage dividers designed to guarantee impedance matching with the coaxial cables. The attenuation factors, as reported in Table I, have been chosen considering that the T1 scintillators are very thin and their outputs have smaller amplitude and width with respect to other scintillators.

As already mentioned, the PMT readout is performed using CITIROC ASICs. For each channel, there are two independently configurable preamplifiers, as illustrated in the block diagram in Fig. 5.

1) The high gain (HG) preamplifier can be set with a gain from 10 to 600.
2) The low gain (LG) preamplifier with gain from 1 to 60.

These two amplification stages allow for acquiring signals produced by particles in a wide energy range: low-mass particles typically produce small signals in TR1 and TR2 scintillators and can be studied using the HG preamplifier. The LG preamplifier, instead, can be used for particles releasing all their energy in the calorimeter and producing larger signals, particularly in the LYSO crystals.

Each preamplifier is followed by a shaper featuring an adjustable shaping time, ranging from 12.5 to 87.5 ns in increments of 12.5 ns. The shaper outputs are connected to an analog memory cell, capable of functioning in two modes.

1) *Track and Hold:* After a trigger is generated, the output of the shaper is sampled after a specific delay determined by a hold signal.
2) *Peak Detection:* After a trigger is generated, the shaper output is followed until the hold signal is provided. The maximum voltage (peak) reached within this time window is then provided in output.

For the HEPD-01, the Track and Hold mode was used since it was the only one available on the EASIROC chip; further details can be found in [17]. In the case of the HEPD-02, the peak detection mode was selected, as suggested by the manufacturer [20], due to different timing characteristics of the various scintillators and the presence of different delays among channels.

TABLE II
DATA PACKET DESCRIPTION

Name	Length (bytes)
Trigger counter	4
Timestamp	4
Trigger ID	1
ADC data	192
Lost trigger	2
Alive time	4
Dead time	4
Trigger flags	8
Turret flags	1
Turret counters	20
Total	240

For each of the 32 channels, the CITIROC generates a trigger signal through a fast shaper and a discriminator with an adjustable threshold (shown in the "Trigger" section of Fig. 5). The 10-bit DACs set a common threshold for all channels, whereas the "4-bit DAC" allows fine-tuning.

The 64 fast trigger signals delivered by the CITIROCs are captured by the FPGA, which generates a global trigger when specific logical conditions, referred to as "trigger masks," are satisfied. Some trigger masks, as in the case of GRB, may require the inclusion of anti-coincidences, i.e., the absence of signals within a relatively long time window up to 90 ns.

For digitization purposes, the CITIROC peak detection system must be armed before the shaped signal reaches the maximum and the CITIROC slow shaping time is set to 50 ns. It is needed then to implement a two-stage trigger. The first stage implements the logic without the anti-coincidence requirements and produces a first-level trigger that is sent back to the CITIROC to arm the peak detection system.

The second stage provides the eventual validation of the first-level trigger if the anti-coincidence request is honored within the 90-ns window. In case of validation, a second-level trigger is generated and the CITIROC analog buffers are digitized; otherwise, the first-level trigger is discarded and the CITIROC analog buffers are cleared.

The global trigger signal enables the readout of the analog outputs of the ASICs and begins the ADC conversion. At the same time, this signal is transmitted to the T-DAQ to initiate the readout process for the direction detector.

The analog output of each amplification chain of the CITIROC is digitized through an ADC, which sequentially reads out the 32 channels following the protocol described in [20]. Two FSMs are designed for this purpose: one controls the CITIROCs analog output and another the ADC conversion.

C. Data Processing and Transmission

The ADC data read from the FPGA are stored in an FIFO along with counters and other data used for the reconstruction of the event. For each event, 240 B of data are produced (see Table II).

Trigger Board data contain the following.

1) *Trigger Counter:* The total number of triggers produced in the current run.
2) *Timestamp:* A 16-μs resolution timestamp.

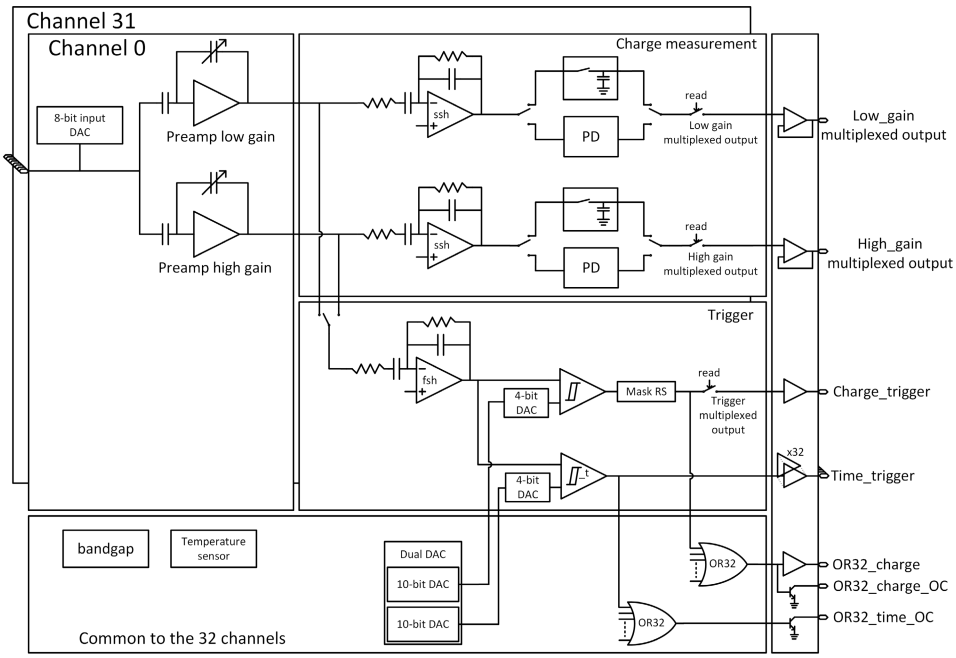

Fig. 5. Block diagram of the CITIROC ASIC by Weeroc. A complete description can be found in [20].

3) *Trigger ID:* An identification number indicating which of the six concurrent trigger masks produced the event trigger.
4) *ADC Data:* The ADC conversions of the 64 channels for both HG and LG preamplifiers.
5) *Lost Trigger:* The number of triggers counted during the previous dead time.
6) *Alive and Dead Time:* Alive and dead time counters (5-μs resolution).
7) *Trigger and Turret Flags:* Flags indicating which TR1 segment is over the threshold. Since the TR1 segments are placed over the direction detector's turrets, these flags also indicate which turrets have been hit by the particle.
8) *Turret Counters:* The number of triggers for each TR1 bar, i.e., the number of triggers transmitted to each tracker's turret.

The data packet is stored in a 62×40 B FIFO, which has a capacity of ten events.

The Trigger Board communicates with the DPCU board using a register-based SpaceWire protocol. The timing diagram in Fig. 6 describes the communication protocol among the three boards.

1) When a trigger is activated, the data generated by the Trigger Board are stored in a FIFO. Additionally, the trigger signal is transmitted to the T-DAQ to initiate its DAQ.
2) If the BUSY signal from the DPCU is not asserted, the first packet in the FIFO is written to a sequence of SpaceWire communication registers.
3) The total length of the data produced is stored in a different register (DATALEN).
4) A DATA_READY signal is sent by the Trigger Board.
5) When the DATA_READY is asserted, the DPCU retrieves the content of the DATALEN register and then reads all the data registers.
6) The DATALEN register is then reset by the DPCU.
7) Once the BUSY signal is deasserted, the following packet in the FIFO (if present) is moved to the communication registers.

IV. Trigger Logic

As shown in Fig. 7 [15], particle fluxes along the CSES satellite orbit vary across several orders of magnitude. The DAQ electronics must ensure the accurate measurement of energy spectra with a high duty cycle.

The Trigger Board supports concurrent trigger configurations to select various particles along the satellite orbit [15].

Each configuration is associated with a prescaling factor tailored to the instrument's data processing and transmission capacity. These configurations are fine-tuned according to scientific requirements, such as the field of view and the type of particle being detected.

The trigger system implements three kinds of trigger masks as follows.

1) *Event Acquisition Masks:* Designed to validate events produced by particles entering the detector from the main window. These masks can be used to select cosmic rays entering the HEPD-02 with increasing energies, meeting different logical conditions.
2) *Event Monitor Masks:* Used for efficiency measurements and to provide information about particles not contained inside the energy detector or entering from the bottom or the side of the detector. A dedicated mask allows evaluating the efficiency of the detector's trigger system in comparison to the event acquisition masks.

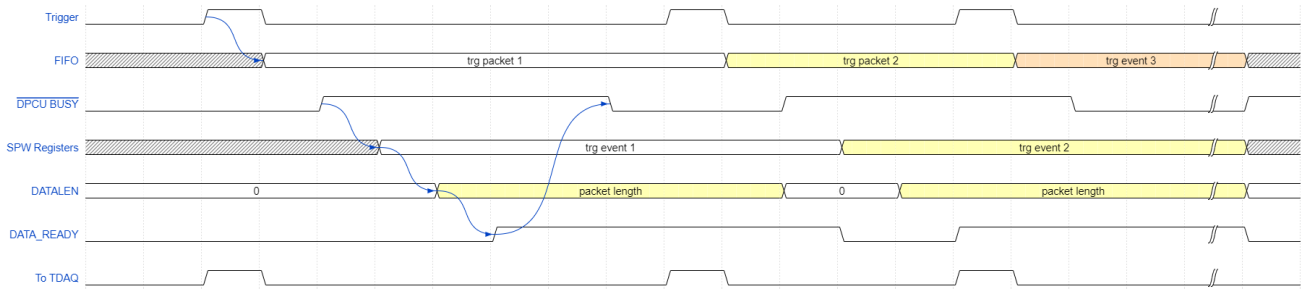

Fig. 6. Time diagram of the interworking protocol for DAQ of the HEPD-02.

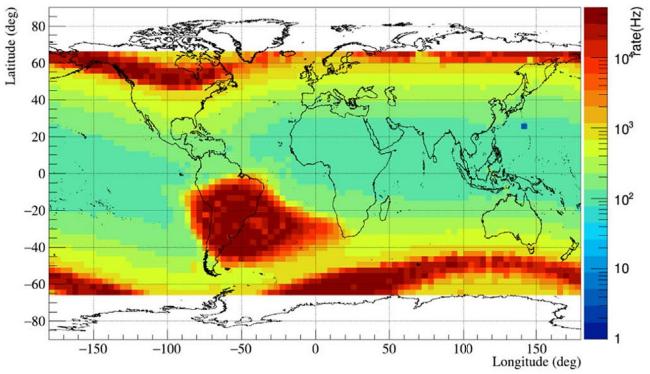

Fig. 7. Count-rate map acquired by the HEPD-01 using the trigger mask, which includes the trigger plane and the first layer of the calorimeter from [15]. This specific trigger mask is the one with the lowest energy threshold, making it particularly sensitive to low-energy electrons from the outer Van Allen belt and low-energy trapped protons in the SAA.

3) *GRB Detection Masks:* Two masks have been implemented to detect GRBs with energies between 2 and 20 MeV. One exploits the high density of the LYSO crystals to detect GRB photons via Compton scattering, while the other is designed for very low-energy photons.

Finally, an additional trigger mask, "generic trigger mask," can be configured to output the logic AND of a selection of any trigger bar or energy detector layer.

The HEPD-02 will be able to operate in concurrence with a selection of six trigger masks. Thanks to the flexibility of the trigger logic, the instrument will be able to collect data on the SAA by selecting the appropriate trigger mask and prescaling factor [21].

The LYSO radioactivity background of the HEPD-02 was measured to explore its sensitivity to gamma rays [22]. It was found that the background has an insignificant impact above 2 MeV, enabling photon counts with a low background rate. The count rates corresponding to the GRB detection masks are checked on a time basis of 5 ms to identify incoming gamma-ray fluxes. The algorithm for GRB detection monitors the GRB rate meters, and it is implemented on the DPCU board. These features enable the HEPD-02 to play a significant role in GRB observation campaigns, offering an exceptionally wide field of view.

The trigger masks enable the investigation of distinct physics scenarios, depending on the satellite's orbital zone. In pursuit of this objective, four distinct orbital zones have been delineated:

1) the SAA (LAT $\in [-60°, 10°]$ and LONG $\in [-90°, 45°]$), in which the fluxes are dominated by trapped electrons at 1 MeV and protons above 8 MeV;
2) the equatorial region (LAT $\in [-35°, 45°]$), where re-entrant and cosmic protons dominate;
3) the outer belt (LAT $\in [-80°, 35°] \cup [45°, 80°]$), where low-energy trapped electrons (below 10 MeV) are expected;
4) the poles ($|\text{LAT}| > 80°$), where primary particle fluxes can be studied.

Given that some regions, like the SAA, experience particle rates as high as approximately 10 MHz, the distribution of data throughput across various physics channels is regulated through trigger prescaling. This approach is implemented to prevent the saturation of the accessible bandwidth.

To enhance the mission physics program, the HEPD-02 will not be restricted to employ just one trigger configuration for each orbital zone; instead, it will have the capability to simultaneously utilize six predefined trigger masks. A set of multiplexers allows the choice of the six trigger masks that are concurrently evaluated. The logical OR of the signals coming from the multiplexers generates the final trigger. Additionally, the output from each multiplexer is stored to ascertain the specific pattern that triggered the event.

The outputs of four of the multiplexers are linked to configurable prescalers, adding a layer of functionality to the setup (see Fig. 8).

V. Functional and Qualification Tests

The Trigger Board has been characterized to verify compliance with system requirements and to define the working parameters that improve the signal acquisition process.

The characterization can be summarized in the following steps:

1) measuring and optimizing the power consumption of the board's power section;
2) assessing threshold levels and minimum signal amplitudes;
3) fine-tuning each stage of the signal conditioning circuit to achieve the maximum dynamic range;
4) developing and implementing new and enhanced algorithms for the trigger logic compared to the HEPD-01.

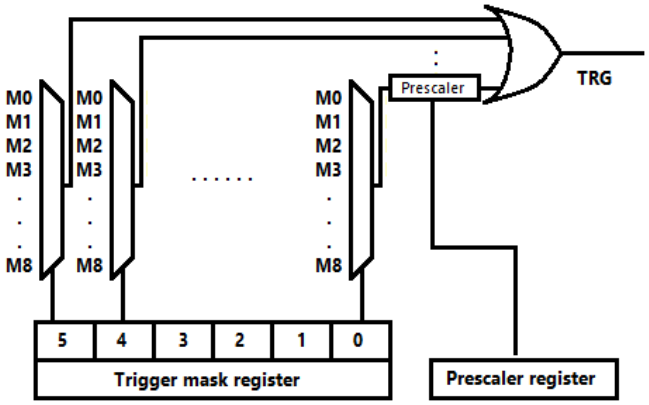

Fig. 8. Scheme of the prescaled concurrent trigger masks. M0–M8 represent different trigger masks.

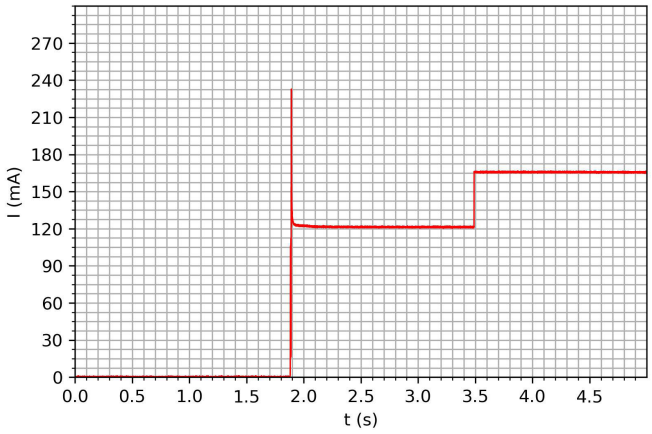

Fig. 9. Power consumption during the first 5 s from the power up.

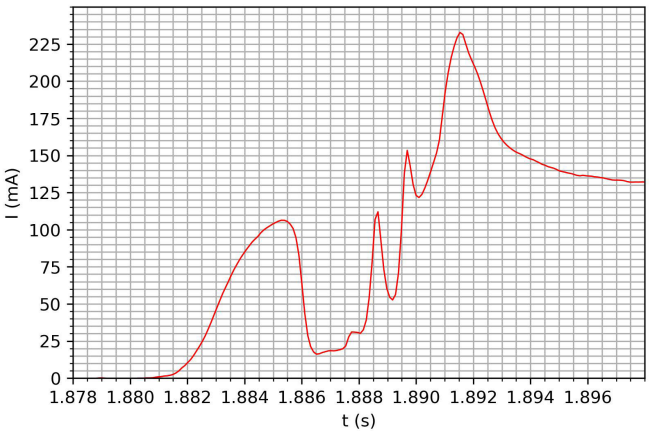

Fig. 10. Detail of the absorption peak at power on.

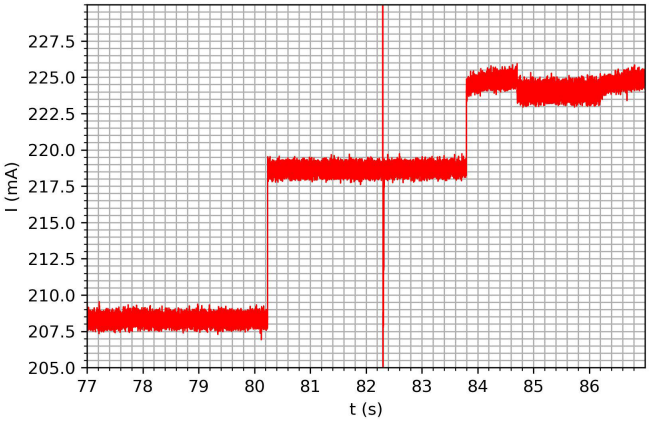

Fig. 11. Power consumption of the Trigger Board with $N_{ch} = 10$.

A. Power Consumption

The power consumption of the Trigger Board may vary based on the number of CITIROC's channels that produce triggers and on their frequency.

For this measurement, a Keysight N6705B power analyzer has been used and a Teledyne T3AWG3352 waveform generator produced the pulses for the board.

Since the pulse generator has only two outputs, a linear fan-in/fan-out (CAEN N401) between the pulse generator and the Trigger Board allowed to increment the number of pulsed channels. Each measurement lasted 90 s and included the power on of the FPGA and the two CITIROCs, the configuration of the working parameters, and 30 s of signal acquisition.

Fig. 9 shows the power consumption at the power on of the Trigger Board. During the first 1.6 s (approximately) since the power on, the watchdog circuit present on the board keeps the reset signal asserted and the current absorption is of 120 mA with a peak at the beginning of 230 mA that lasts about 23 ms. This peak is caused by the inrush current. After the reset is deasserted, the current rises to 160 mA (see Figs. 9 and 10).

B. Multiple-Channel Consumption

A first test was carried out using two to ten channels of the board and stimulating them with square signals of 10 ns and 3 V with a frequency of 8 MHz. The test was performed using the TR1 · TR2 trigger mask, prescaled to 8000 to simulate the worst-case scenario of a very high particle rate that triggers various channels of the CITIROCs, requiring the detector trigger rate to be limited. An example of the board current absorption when ten channels are stimulated is depicted in Fig. 11. The first rise in the current corresponds to the enabling of the pulse generator output that produces the CITIROC's single-channel triggers. The second increment is related to the start of the acquisition after the production of the global trigger. The peak around 82 s corresponds to the configuration of the CITIROCs' parameters, which happens just before the start of acquisition and after the enabling of the pulse generator. The little variations after the last step correspond to the transfer of data and signals to the DPCU.

The values of current absorption are reported in Table III.

It is possible to fit these values to obtain the relationship between the current absorption and the number of pulsed channels

$$I(N_{ch}) = 0.6 \cdot N_{ch} + 219. \quad (1)$$

TABLE III
POWER CONSUMPTION OF THE TRIGGER BOARD AT DIFFERENT NUMBERS OF PULSED CHANNELS

N_{ch}	I (mA)	σ_I (mA)
2	219.1	0.5
4	222.3	0.4
6	222.7	0.5
8	223.6	0.5
10	224.4	0.5

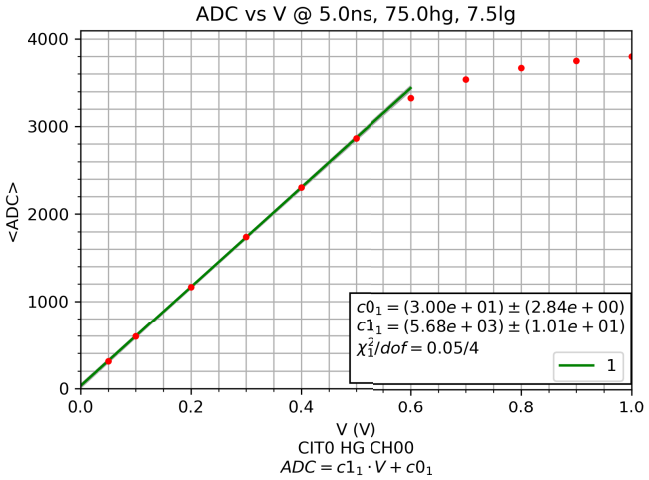

Fig. 12. ADC versus V for TR1-like signals (HG = 75).

This expression brings to a maximum current absorption (when 64 channels are producing single-channel trigger signals) of 260 mA that corresponds to the maximum power consumption of 3.12 W, still within the design limits.

C. Calibration of the CITIROC's Preamplifiers

A series of measurements has been made varying the gain of the preamplifiers and the shaping time.

Some examples of the final results of this work are shown in Figs. 12–14 that report the mean ADC counts as a function of the signal amplitude in volts.

The used input signals are square pulses with different durations, which has been chosen considering the full-width at half-maximum (FWHM) of the typical signal produced by the PMTs for a different type of scintillators: 5 ns for TR1 counters, 10 ns for the plastic scintillators, and 50 ns for the LYSO crystals.

We used a shaping time of 50 ns common to all the channels. The amplification for the channels related to all the plastic scintillators was set to 75 for the HG and 7.5 for the LG, while the LYSO channels were set with a gain of 10 for HG preamplifiers and 1.5 for LG.

After the detector integration, crosstalk between channels was observed when particles produced high-amplitude signals in a large number of scintillators.

This effect was not present in the laboratory measurement on the board and led to a change in the selected gain for the preamplifiers of the channels connected with TR1 and the calorimeter.

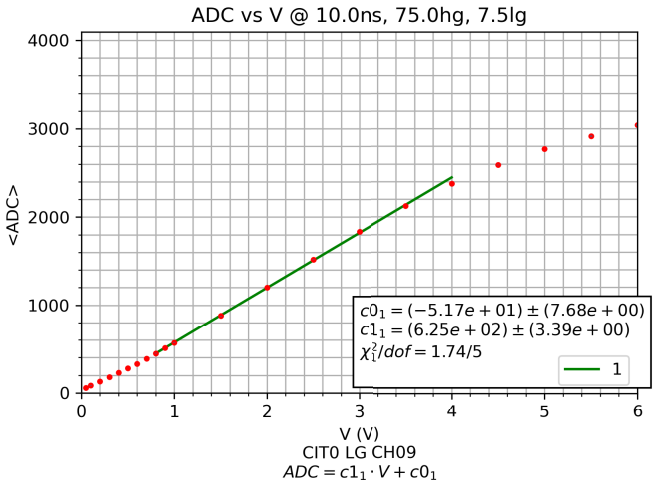

Fig. 13. ADC versus V for CALO-like signals (LG = 7.5).

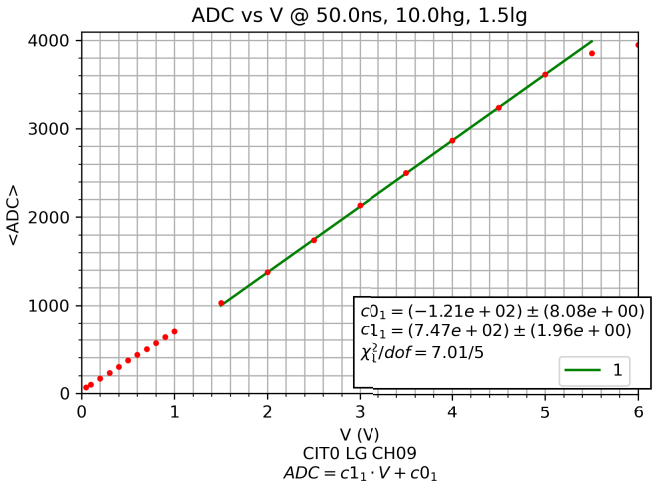

Fig. 14. ADC versus V for LYSO-like signals (LG = 1.5).

TABLE IV
FLIGHT VALUES FOR THE PREAMPLIFIERS' GAIN OF THE CITIROC

Board channels	Scintillators	HG	LG
0 - 4, 32 - 36	TR1	20	2
5 - 20, 27 - 31, 37 - 52, 59 - 63	TR2, RAN BOT, LAT	20	2
21 - 26, 53 - 58	EN	10	1.5

The selected values for the preamplifier gain are shown in Table IV, and the related calibration curves for CALO-like signals are shown in Figs. 15 and 16, reporting the mean ADC counts as a function of the charge injected into the board channel. Since the LYSO channel configuration did not change, only the plastic scintillator channels are reported.

D. Slow Shaper Calibration

The experimental setup used to calibrate the CITIROC's slow shapers is described as follows: the first channel of the pulse generator has been connected to the "External trigger"

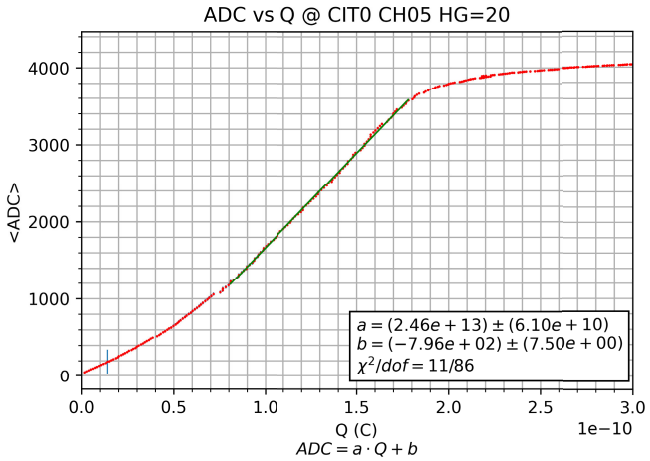

Fig. 15. ADC versus Q for CALO-like signals (HG = 20).

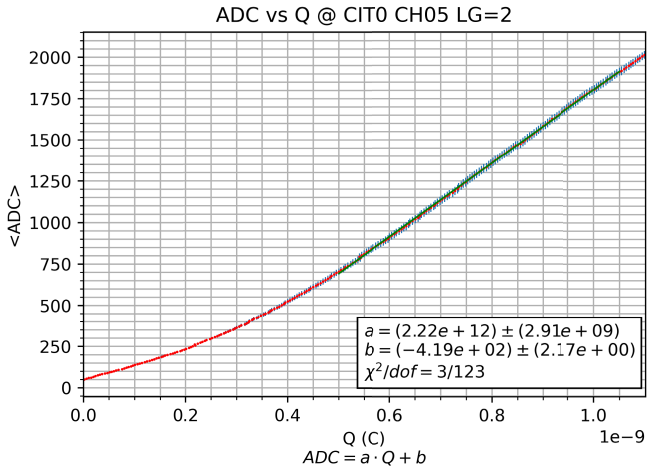

Fig. 16. ADC versus Q for CALO-like signals (LG = 2).

input of the board and the second channel has been connected to the CH05 (with attenuation equal to 12) of the Trigger Board. The measurement has been repeated for different preamplifier gains but only the plots obtained with gains of 20 for HG and two for LG will be reported.

We used 50-mV square signals with increasing duration (T) for different values of the shaping time (T_{shap}). In this way, it is possible to study the shaper behavior when the width of an input signal approaches to the selected T_{shap}. In Fig. 17, the ADC versus T plots is shown for T_{shap} equal to 50 ns. From this plot, it is clear that the shapers work linearly until the widths of the input signals are comparable with the shaping time.

Fig. 18 shows the plot of the relative differences between the ADC distribution's most probable values (MPVs) and the values predicted from the linear regression. Considering signal widths that ensure residuals below 5%, from Table V, it is possible to see that the extrapolated values are close to the nominal ones. A shaping time of 50 ns was chosen as the default configuration during the normal operation of the detector.

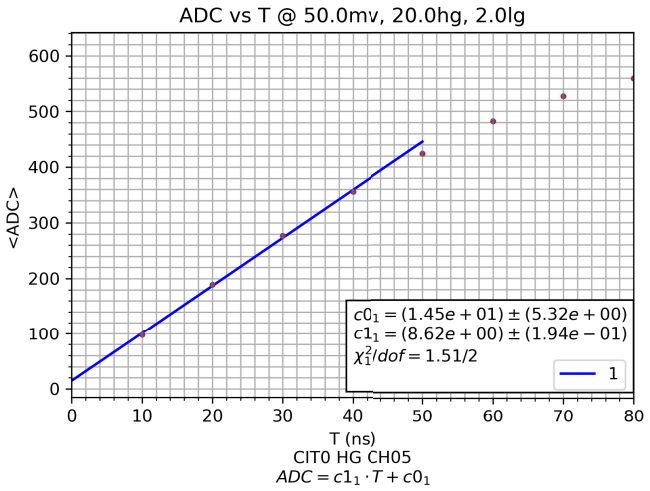

Fig. 17. HG shaper calibration, $T_{\text{shap}} = 50$ ns.

TABLE V
NOMINAL AND EXTRAPOLATED SHAPING TIMES

$T_{nominal}$ (ns)	T_{extr} (ns)	
	HG	LG
25	30	30
50	50	65
62.5	60	75
87.5	80	90

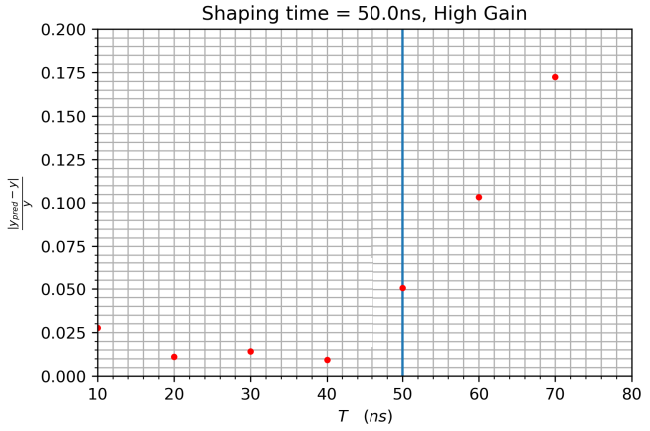

Fig. 18. HG shaper relative residuals, $T_{\text{shap}} = 50$ ns.

E. Peak Detection Time Window Tuning

The CITIROC peak detection circuit requires an HOLD signal that disconnects the analog memory circuit from the slow shaper output and allows it to store it in a capacitor.

The HOLD signal must be delayed for the correct functioning of the peak detector and, most importantly, to ensure that all the scintillator signals have the time to reach their maximum value when a trigger occurs. This is obtained with a flip-flops chain that produces 160 ns of delay.

To this time, 40 ns must be added for the trigger signal to be produced, 10 ns to be expanded, and other 10 ns to produce the HOLD signal. This brings to a time window of 220 ns,

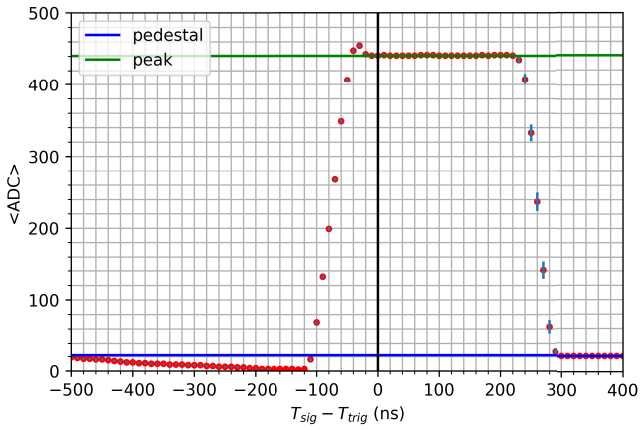

Fig. 19. Validation of the peak detection time window.

TABLE VI
SCINTILLATOR'S TYPICAL MIP AND MIP/3 SIGNALS AND SNR

Scintillator	FWHM (ns)	MPV		3 percentile			
		MIP V (mV)	MIP/3 V (mV)	MIP V (mV)	MIP SNR	MIP/3 V (mV)	MIP/3 SNR
TR1	5	88	29	51	14.5 ± 0.4	17	1.9 ± 0.1
Calorimeter	10	120	40	81	30.9 ± 0.4	27	7.5 ± 0.1
LYSO	50	216	72	114	167 ± 5	38	51 ± 1

during which the peak detector memorizes the slow shaper peak.

To validate this time window, we connected a dual-channel pulse generator to the external trigger input and CH05, adjusting the delay between the channels. Pulses of 200 mV and 10 ns have been used with a frequency of 20 Hz. Fig. 19 shows the ADC counts as a function of the delay between the external trigger signal and the CH05 signal.

It is possible to see that the ADC counts stay constant up to $\Delta T = +220$ ns and then decrease. The decrease is caused by the slow shaper signal gradually exiting from the peak detector window.

For negative ΔT (i.e., when the signal on CH05 anticipates the external trigger signal), ADC counts below the pedestal can be observed. This effect can be attributed to the undershoot of the slow shaper signal, which causes a slight discharge of the analog memory capacitor.

From this consideration, it is possible to observe that two consecutive signals, on the same channel of the board, can be considered independent if they are delayed at least by 500 ns.

F. SNR Measurements

With the defined gains and shaping time, the signal-to-noise ratio (SNR) has been measured.

For this measurement, the distribution of signals produced by cosmic muons on different scintillators has been considered. In Table VI, the amplitude of minimum ionizing particle (MIP), 1/3 MIP, and the values of the 3% of the distributions are reported.

Using the external trigger and the channels CH00 and CH05 (with attenuation of 6 and 12, respectively), the Trigger Board has been pulsed with signals with amplitudes corresponding

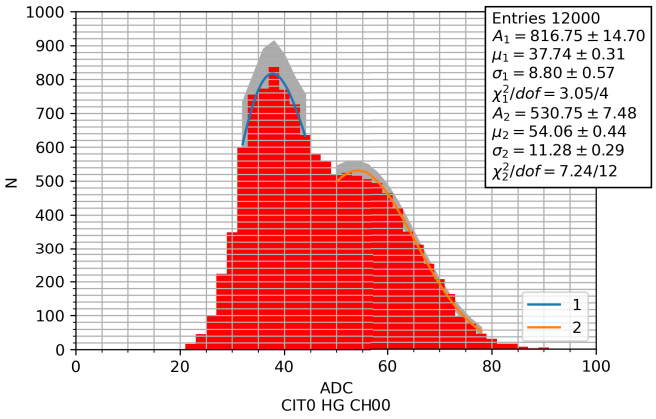

Fig. 20. TR1-like signals: 1/3 MIP HG = 20, attenuation = 6, line 1 represents the pedestal fit, and line 2 represents the signal fit.

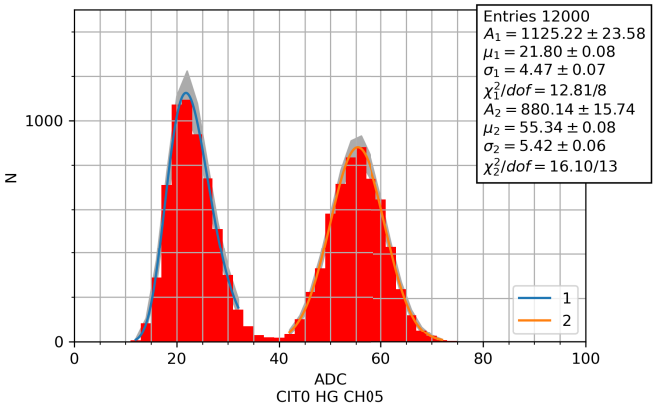

Fig. 21. CALO-like signals: 1/3 MIP HG = 20, attenuation = 12, line 1 represents the pedestal fit, and line 2 represents the signal fit.

to the value of the 3% of the distribution for 1/3 MIP, derived from the acquisition of cosmic muons.

Figs. 20–22 show the ADC count distribution for two of the three types of signals. In Table VI, the SNR values, obtained with the following expression are reported:

$$\text{SNR} = \frac{\mu_{\text{sig}} - \mu_{\text{pdst}}}{\sigma_{\text{pdst}}}. \tag{2}$$

The SNR values are always good for 1 MIP whereas TR1 scintillators' signals corresponding to one-third of MIP are hardly distinguishable from noise. This is not a real issue since the TR1 scintillators are almost always used in coincidence with the other scintillators or, in the case of the lowest energy mask, validated by the tracker.

G. Threshold Calibration

A threshold scan at different input signal amplitudes has been made to find a correspondence between the DAC value set for the threshold and the amplitude of the input signal that generates a trigger. As can be seen from the plot, the trigger efficiency decreases with the increase of the DAC value set on the CITIROC discriminator.

Fig. 23 shows an example of an S-curve obtained using pulses of 40 mV and 50 ns and a frequency of 1 kHz and increasing the threshold's DAC value.

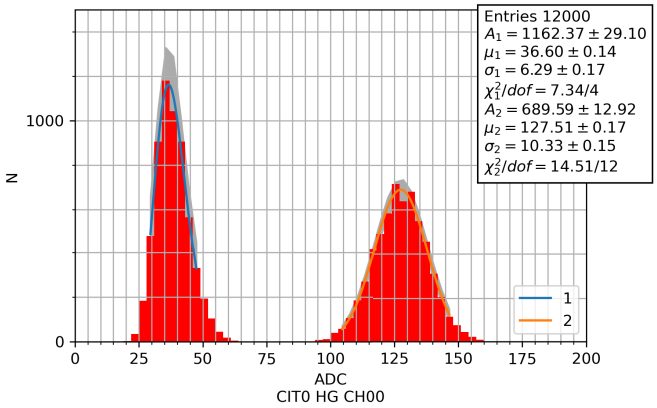

Fig. 22. TR1-like signals: 1 MIP HG = 20, attenuation = 6, line 1 represents the pedestal fit, and line 2 represents the signal fit.

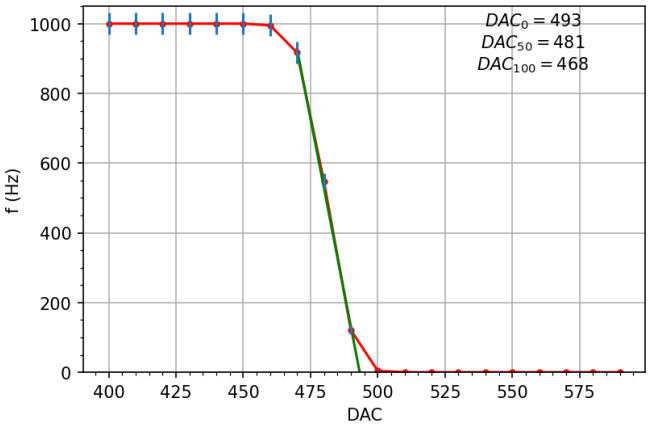

Fig. 23. *S*-curve acquired with a signal of 40 mV, 50 ns at 1 kHz.

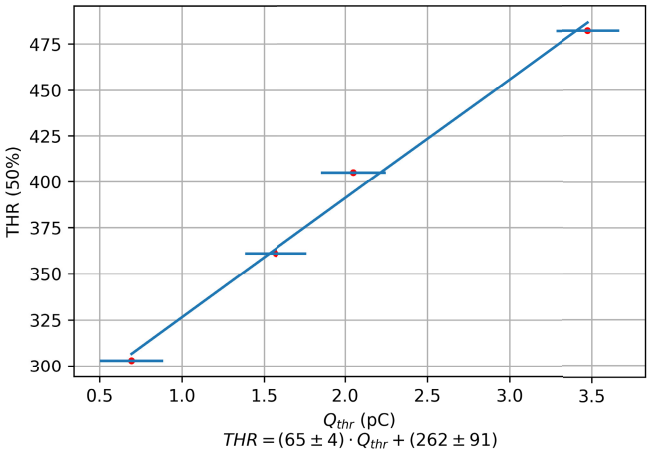

Fig. 24. Threshold DAC values (THR) as a function of the input signal (Q_{thr}) for TR1-like signals.

Repeating this measurement for the three different types of signals (TR1-like, calorimeter-like, and LYSO-like) and for different amplitudes, we obtained plots like the one shown in Fig. 24. These plots show the threshold values that bring the trigger efficiency to 50% as a function of the input signal.

VI. Conclusion

The Trigger Board of the HEPD onboard the second CSES has been designed, developed, and extensively tested to optimize its performance for space applications. We presented the design, architecture, and functionality of the trigger and calorimeter DAQ system, highlighting its advancements over its predecessor, the first HEPD.

Key improvements include the following:

1) enhanced trigger logic, enabling simultaneous use of multiple trigger masks and prescaled event selection to optimize DAQ across different orbital regions;
2) improved signal processing, with optimized preamplifier gains, shaping times, and a peak detection algorithm, ensuring precise measurement of particle interactions;
3) versatility for scientific observations, supporting the detection of cosmic rays, trapped radiation, and GRBs with a high-duty cycle and low background noise.

These advancements permit the detector to operate efficiently in challenging regions like the SAA and polar regions, broadening the mission's scientific scope.

The supplementary capabilities, such as integrating concurrent and prescaled triggers, have undergone rigorous testing and demonstrated consistent performance as expected.

Extensive laboratory and beam tests validated the system's power efficiency, signal-to-noise performance, and threshold calibrations, confirming compliance with mission requirements. These enhancements ensure that the second HEPD will operate reliably in space, enabling high-precision studies of the radiation environment, space weather, and potential seismic precursors.

In addition, as for the first HEPD [23], the whole detector underwent thorough a calibration procedure at accelerator laboratories, which was performed on two identical models, the so-called qualification and flight models, before the delivery to China for final integration, to characterize the energetic response of the detector necessary for in-flight particle-flux reconstruction.

Acknowledgment

This work was supported by the Italian Space Agency in the framework of the ?Accordo Attuativo 2020-32.HH.0 Limadou Scienza+? (CUP F19C20000110005) and the ASI-INFN agreement n.2014-037-R.0, addendum 2014-037-R-1-2017.

References

[1] X. Shen et al., "The state-of-the-art of the China seismo-electromagnetic satellite mission," *Sci. China Technol. Sci.*, vol. 61, no. 5, pp. 634–642, May 2018, doi: 10.1007/s11431-018-9242-0.

[2] G. Ambrosi et al., "The HEPD particle detector of the CSES satellite mission for investigating seismo-associated perturbations of the van Allen belts," *Sci. China Technol. Sci.*, vol. 61, no. 5, pp. 643–652, May 2018, doi: 10.1007/s11431-018-9234-9.

[3] F. Palma et al., "The August 2018 geomagnetic storm observed by the high-energy particle detector on board the CSES-01 satellite," *Appl. Sci.*, vol. 11, no. 12, p. 5680, Jun. 2021, doi: 10.3390/app11125680.

[4] M. Piersanti et al., "Magnetospheric-ionospheric-lithospheric coupling model. 1: Observations during the 5, Aug. 2018 Bayan Earthquake," *Remote Sensing*, vol. 12, no. 20, 2020, doi: 10.3390/rs12203299.

[5] M. Akhoondzadeh, A. De Santis, D. Marchetti, and X. Shen, "Swarm-TEC satellite measurements as a potential earthquake precursor together with other swarm and CSES data: The case of Mw7.6 2019 Papua new Guinea seismic event," *Frontiers Earth Sci.*, vol. 10, Feb. 2022, doi: 10.3389/feart.2022.820189.

[6] M. Martucci et al., "Trapped proton fluxes estimation inside the south Atlantic anomaly using the NASA AE9/AP9/SPM radiation models along the China seismo-electromagnetic satellite orbit," *Appl. Sci.*, vol. 11, no. 8, p. 3465, Apr. 2021, doi: 10.3390/app11083465.

[7] S. Bartocci et al., "Mapping the south Atlantic anomaly charged particle environment with the HEPD-01 detector on board the CSES-01 satellite," *Phys. Rev. D, Part. Fields*, vol. 111, no. 2, Jan. 2025, doi: 10.1103/physrevd.111.022001.

[8] M. Martucci et al., "Time dependence of 50–250 MeV galactic cosmic-ray protons between solar cycles 24 and 25, measured by the high-energy particle detector on board the CSES-01 satellite," *Astrophysical J. Lett.*, vol. 945, no. 2, p. L39, Mar. 2023, doi: 10.3847/2041-8213/acbea7.

[9] M. Martucci et al., "The first ground-level enhancement of solar cycle 25 as seen by the high-energy particle detector (HEPD) on board the CSES-01 satellite," *Space Weather*, vol. 21, no. 1, Jan. 2023, Art. no. 022001, doi: 10.1029/2022sw003191.

[10] F. Palma et al., "Gamma-ray burst observations by the high-energy particle detector on board the China seismo-electromagnetic satellite between 2019 and 2021," *Astrophysical J.*, vol. 960, no. 1, p. 21, Jan. 2024, doi: 10.3847/1538-4357/ad06ae.

[11] R. Battiston et al., "Observation of anomalous electron fluxes induced by GRB221009A on CSES-01 low-energy charged particle detector," *Astrophysical J. Lett.*, vol. 946, no. 1, p. 29, Mar. 2023, doi: 10.3847/2041-8213/acc247.

[12] S. Bartocci et al., "The catalogue of gamma-ray burst observations by HEPD-01 in the 0.3–50 MeV energy range," *Astrophysical J.*, vol. 976, no. 2, p. 239, Dec. 2024, doi: 10.3847/1538-4357/ad822c.

[13] G. Ambrosi et al., "The electronics of the high-energy particle detector on board the CSES-01 satellite," *Nucl. Instrum. Methods Phys. Res. A, Accel. Spectrom. Detect. Assoc. Equip.*, vol. 1013, Oct. 2021, Art. no. 165639, doi: 10.1016/j.nima.2021.165639.

[14] V. Scotti, "Trigger and data acquisition system of the high energy particle detector on board the CSES-02 satellite," *Nucl. Instrum. Methods Phys. Res. A, Accel. Spectrom. Detect. Assoc. Equip.*, vol. 1046, Jan. 2023, Art. no. 167741, doi: 10.1016/j.nima.2022.167741.

[15] P. Picozza et al., "Scientific goals and in-orbit performance of the high-energy particle detector on board the CSES," *Astrophysical J. Suppl. Ser.*, vol. 243, no. 1, p. 16, Jul. 2019, doi: 10.3847/1538-4365/ab276c.

[16] S. Bartocci et al., "Galactic cosmic-ray hydrogen spectra in the 40–250 MeV range measured by the high-energy particle detector (HEPD) on board the CSES-01 satellite between 2018 and 2020," *Astrophysical J.*, vol. 901, no. 1, p. 8, Sep. 2020, doi: 10.3847/1538-4357/abad3e.

[17] V. Scotti, M. Mese, and G. Osteria, "A versatile readout and trigger system for the high energy particle detector onboard the satellite CSES-02," in *Proc. IEEE Nucl. Sci. Symp. Med. Imag. Conf. (NSS/MIC)*, Apr. 2019, pp. 1–3, doi: 10.1109/NSS/MIC42101.2019.9059936.

[18] S. Bartocci et al., "The scintillation counters of the high-energy particle detector of the China seismo-electromagnetic (CSES-02) satellite," *Remote Sens.*, vol. 16, no. 21, p. 3982, Oct. 2024, doi: 10.3390/rs16213982.

[19] M. Mese et al., "The PMT acquisition and trigger generation system of the HEPD-02 calorimeter for the CSES-02 satellite," *Instruments*, vol. 7, no. 4, p. 53, Dec. 2023, doi: 10.3390/instruments7040053.

[20] *Citiroc User Guide*. Accessed: Apr. 7, 2025. [Online]. Available: https://www.weeroc.com/products/sipm-read-out/citiroc-1a

[21] M. Martucci et al., "New results on protons inside the south Atlantic anomaly, at energies between 40 and 250 MeV in the period 2018–2020, from the CSES-01 satellite mission," *Phys. Rev. D, Part. Fields*, vol. 105, no. 6, Mar. 2022, Art. no. 062001, doi: 10.1103/physrevd.105.062001.

[22] S. Perciballi et al., "Performance of the HEPD-02 LYSO calorimeter and expected sensitivity to GRBs detection," *Proc. Sci.*, vol. 395, p. 583, Jun. 2021, doi: 10.22323/1.395.0583.

[23] G. Ambrosi et al., "Beam test calibrations of the HEPD detector on board the China seismo-electromagnetic satellite," *Nucl. Instrum. Methods Phys. Res. A, Accel. Spectrom. Detect. Assoc. Equip.*, vol. 974, Sep. 2020, Art. no. 164170, doi: 10.1016/j.nima.2020.164170.